

> REPLACE THIS LINE WITH YOUR MANUSCRIPT ID NUMBER (DOUBLE-CLICK HERE TO EDIT) <

Geometric Calibration for the Linear Array Camera Based on Star Observation

Zhichao Guan, Yonghua Jiang*, Guo Zhang, Xing Zhong

Abstract—This study presents an innovative geometric calibration mode for a linear array camera used in the Jilin-1 satellite. Changing the camera from observing the ground to observing space and treating stars as control points (SCPs) allow for the accurate determination of the geometric parameters of the camera. In this study, several important calibration procedures and strategies are presented to gradually eliminate the influence of astronomical and attitude errors. Self-verification of the calibration image results in a star-based calibration accuracy is better than 0.3 pixels. Further verification of the star image leads to an interior orientation accuracy is better than 0.6 pixels. The accuracy of geometric positioning without control is verified by ground images of different regions to be 30 m. The interior orientation accuracy of ground images processed by star-based calibration parameters is better than 1.5 m. The ground image corrected using the star-based calibration parameters is well overlaid on the reference image. The accuracies obtained with star-based and ground-based calibrations are comparable. However, ground calibration fields require high maintenance costs and may suffer from harsh imaging conditions. Contrarily, star-based calibration is not affected by the weather and climate conditions on the ground, which can be photographed from any location along the satellite orbit. Therefore, star-based calibration can meet the requirements for high-frequency geometric calibration of subsequent satellite constellations construction.

Index Terms—Geometric calibration; Jilin-1; Linear array camera; Star observation; Satellite constellations.

I. INTRODUCTION

WITH the improvements in platform and payload technologies, the total weights of satellites gradually decrease. To improve the efficiency of satellite observation, institutions and companies in various countries are starting to build Earth observation satellite constellations. The constellations can provide rich remote sensing data and rapid product services for global land use, surface vegetation cover, precision agriculture, three-dimensional reality, disaster warning, emergency response, etc. High-resolution linear array optical cameras are the main source of data acquisition for Earth observation satellite systems owing to their high signal-to-noise ratios. Moreover, well-calibrated images are the basis for subsequent satellite fusion processing and data application [1]. Typically, before a satellite is launched, the camera and other

loads are geometrically calibrated on the ground. However, after the satellite enters orbit, the relative relationship between the various loads needs to be recalibrated because of mechanical vibration, temperature variations, and other factors [2], [3]. At the same time, the geometric parameters of the linear array camera may change over time, resulting in significant degradation of the geometric positioning accuracy [4], [5]. Therefore, satellites need to be calibrated regularly throughout their in-orbit lifetime to maintain the geometric quality of the product. Furthermore, it is necessary to find a simple and reliable way to perform the geometric calibration of the camera in a quick and timely manner to meet the product requirements of satellite constellation construction and the future application of AI [6], [7].

Currently, the ground-imaging method is mainly used for the geometric calibration of optical remote sensing cameras. This method mainly includes three ways. The first involves manually deploying targets. The calibration targets are manually set up beforehand in a large area in the satellite transit region, and the geometric calibration of the camera is performed by selecting the target on the image. The second way involves the imaging of a digital calibration field. The geometric calibration of the camera is achieved by a high-precision matching between the image and the digital calibration field [8], [9], [10]. The third way involves photographing the flat ground at specific multiple angles. The geometric calibration of the camera is achieved by the self-reflection characteristics of errors [11], [12], [13], [14], [15], [16]. The above three methods all achieve geometric correction by photographing the ground and are uniformly referred to as the “ground observation mode”. However, owing to factors such as weather, illumination, terrain, resolution, spectrum, viewing angle, and changes in ground conditions, the first and second methods are costly and time-consuming. Additionally, the third method depends heavily on the accuracy of the matching algorithm. The above defects make it impossible to quickly and timely perform geometric calibration in the “ground observation mode”.

In this study, we innovatively proposed a geometric calibration method for linear array cameras based on the “star observation mode”. Under reasonable imaging conditions, we can directly image stars with optical cameras [17], [18], [19].

This work was supported by the National Natural Science Foundation of China (NSFC) under grants 42301424 and 42171341. (*Corresponding author: Yonghua jiang.*)

Zhichao Guan is with the National Satellite Meteorological Center (NSMC), China Meteorological Administration, Beijing, China (e-mail: guanzc@cma.gov.cn, guanzhichao@whu.edu.cn), and the State Key Laboratory of Information Engineering in Surveying, Mapping and Remote Sensing

(LIESMARS), Wuhan University, Wuhan, China. Yonghua Jiang is with the School of Remote Sensing and Information Engineering, Wuhan University, Wuhan, China (e-mail: jiangyh@whu.edu.cn). Guo Zhang is with the LIESMARS, Wuhan University, Wuhan, China (e-mail: guozhang@whu.edu.cn). Xing Zhong is with the Chang Guang Satellite Technology Co., Ltd., Changchun, China (e-mail: ciomper@163.com).

> REPLACE THIS LINE WITH YOUR MANUSCRIPT ID NUMBER (DOUBLE-CLICK HERE TO EDIT) <

The coordinates of stars in the celestial coordinate system are known that we can use the stars as control points to calibrate the cameras.

Fig. 1 shows a schematic diagram of the ground and star observation modes for a linear array camera. Assume that the camera coordinate system is $(O - XYZ)_{cam}$, and the inertial space coordinate system where the satellite is located is $(O - XYZ)_{J2000}$. In the ground observation mode, the satellite overcomes the Earth's rotation by adjusting the drift angle (the Z_{cam} axis of the camera). Then, the satellite will slowly push broom the pitch axis (the Y_{cam} axis of the camera) to obtain a normal ground image (as shown in Fig. 1, labels *abcd*). In the star observation mode, it is necessary to push broom the satellite

pitch axis (the Y_{cam} axis of the camera) at a certain angular velocity to satisfy the time-delayed integration (TDI) conditions of the linear array camera and eventually obtain a star image. The push broom begins with $A'B'$ at time t_{i-1} , and ends with CD at time t_{i+1} . In Fig. 1, $A'B'CD$ mark the pushing area of the linear array camera, and the black pentagram is a star. Because the distance of stars can be considered infinite, the position of the stars in the image is related only to the attitude change and not to the orbit change of the satellite. The final imaging area is actually $ABCD$, that is, the area covered by the equivalent rotation angle φ , where the surface ABO_{cam} is parallel to the surface $A'B'O_{cam}$. The red pentagram represents the actual star distribution in the star image.

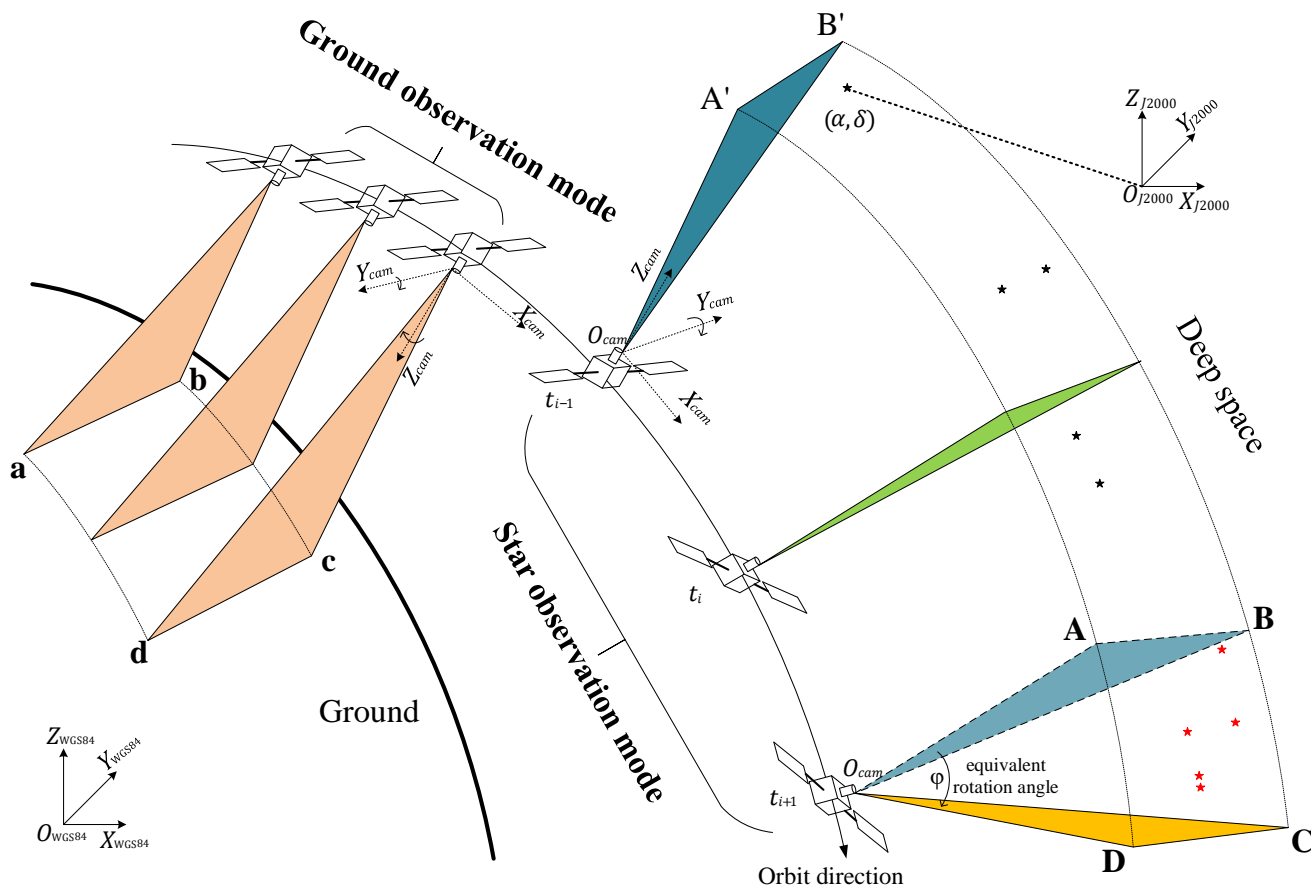


Fig. 1. Schematic diagram of the ground and star observation modes for a linear array camera

The star observation mode has many obvious advantages, for which we have summarized six aspects. Firstly, available anytime. The ground observation mode can only photograph ground during the daytime, while the satellite can use its idle time in the Earth's shadow area to photograph stars through the star observation mode. Secondly, no weather impact. When a satellite observing stars, factors such as rain, snow, cloudy on the ground do not affect the camera. Thirdly, anywhere is fine. The land area accounts for less than 30% of the Earth's surface, while stars are distributed throughout the entire celestial sphere. Fourth, high precision. The coordinates of stars in the star catalog are precisely known, with an accuracy better than

0.00012", making it an ideal absolute control point source [19]. Fifth, low cost. The star observation mode reducing the construction and maintenance costs of the ground calibration field. Sixth, it can be integrated into satellites on-orbit system. Ground images from different angles and seasons have a significant impact on the matching efficiency and accuracy when calibration. But stars are point targets in images, and their recognition algorithms are more robust. When this technology matures, star-based geometric calibration algorithms can be deployed on satellites.

Currently, the research of camera calibration based on star observation is an important research direction. In the image

> REPLACE THIS LINE WITH YOUR MANUSCRIPT ID NUMBER (DOUBLE-CLICK HERE TO EDIT) <

processing method of the Pléiades satellite, Greslou et al. mentioned that the use of star observation can enable the geometric and radiative calibration of the camera [17], [18]. However, later studies only examined radiative calibration using star observation, and no articles or experimental results on geometric calibration have been published [21]. In a previous work, we used star observation to calibrate the area array cameras of several satellites and achieved the calibration of the installation parameters of the camera by photographing stars with the Luojia 1 night-light satellite [5]. Later, we also demonstrated the feasibility of calibrating the interior orientation parameters of the area array camera using the star map data from Ziyuan-3 [22]. Subsequently, the Jilin-1 video area array camera was used to observe stars at different orbital positions to achieve long-term monitoring of the exterior orientation parameters between star trackers and cameras [23], [24]. Li et al. proposed a correction method based on star observations to correct the exterior orientation error of a geostationary area array camera caused by spatial thermal deformation [25]. Jiang et al. developed a geometric calibration method using the relative motion of stars for geostationary cameras and calibrated the relative installations of the camera [26]. Chen et al. also achieved geometric calibration of the Jilin-1 video satellite by using sequence images of the star observation and achieved interior calibration of the area array camera [27].

For area array cameras, stars are acquired simultaneously within each image. The satellite attitude error of each image is consistent. Therefore, the interior and exterior orientations parameters of area array cameras are stable to solve when doing geometric calibration. For linear array cameras, the imaging time of each line is different, that is, each star has a different

satellite attitude error. Therefore, for the calibration of linear array cameras, the error caused by the non-stationary satellite attitude must be considered. Further, because the star coordinates are not fixed in the inertial coordinate system, their astronomical errors must be corrected.

The remainder of this paper is structured as follows. The geometric calibration method of star observation of linear array cameras is constructed in Section II. The experimental data from the Jilin-1 satellite and star catalog are presented in Section III. The processed star observation data are presented in Section IV. The geometric accuracy of the star-based calibration is discussed in detail in Section V. Finally, in Section VI we outline our conclusions and provide some remarks.

II. METHODS

The entire process of star observation and calibration for linear array cameras is shown in Fig. 2. In Section A, a geometric model for star observation of linear array cameras is constructed. Section B is an introduction to the precise extraction of star control points (SCPs). The coordinates of stars on the image side are obtained through stripe background noise elimination and star point extraction. The coordinates of stars on the object side are obtained by geometric model prediction and astronomical coordinate correction which is a key factor of our method. These processes provide high-precision SCPs. Section C introduces the geometric calibration model for star observation. This mainly includes the construction of geometric calibration models and equivalent distortion models. The correction strategies for the non-stationary attitude of the linear array camera are another key factor of our method.

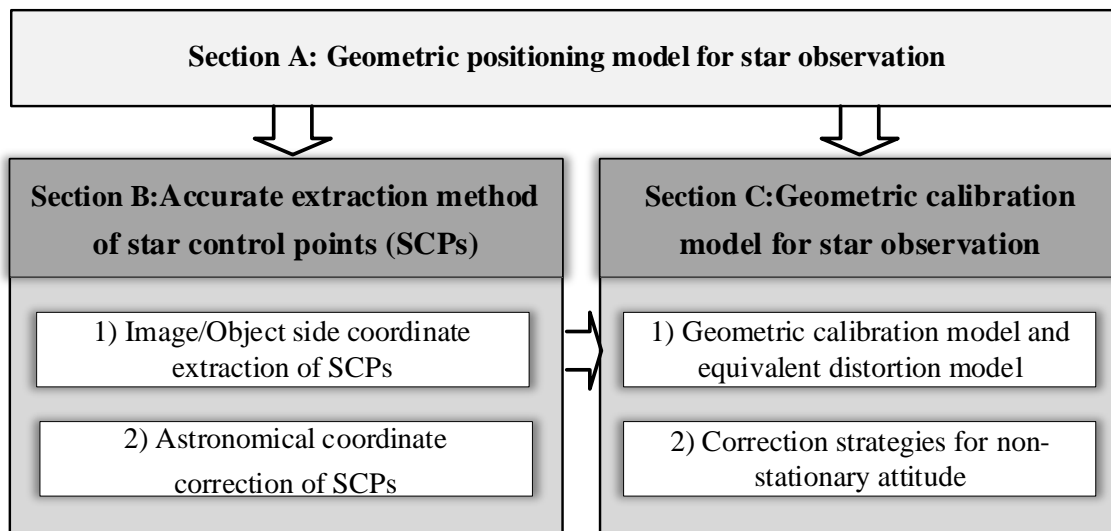


Fig. 2. Geometric calibration process for star observation with a linear array camera

A. Geometric positioning model for star observation

Suppose that, at the time of t_i , the coordinates of the star in the image plane coordinate system XOY are (x, y) (see Fig. 1). Then, the direction of the star (\mathbf{W}) in the camera coordinate

system is:

> REPLACE THIS LINE WITH YOUR MANUSCRIPT ID NUMBER (DOUBLE-CLICK HERE TO EDIT) <

$$\mathbf{W} = \frac{1}{\sqrt{(x-x_0)^2 + (y-y_0)^2 + f^2}} \begin{bmatrix} x-x_0 \\ y-y_0 \\ -f \end{bmatrix} = m \begin{bmatrix} x-x_0 \\ y-y_0 \\ -f \end{bmatrix} \quad (1)$$

where f and (x_0, y_0) are the principal distance and coordinates of the camera, respectively. m is the zoom factor. Suppose that the attitude of the camera coordinate system in the inertial coordinate system at time t_i is $\mathbf{R}_{Cam}^{J2000}(t_i)$. Then, the direction of the star (\mathbf{Z}) in the inertial coordinate system is:

$$\mathbf{Z} = \mathbf{R}_{Cam}^{J2000}(t_i) \mathbf{W} \quad (2)$$

If we decompose the star coordinate direction into the right ascension and declination (α, δ) , then:

$$\mathbf{Z} = \begin{bmatrix} \cos\alpha \cdot \cos\delta \\ \sin\alpha \cdot \cos\delta \\ \sin\delta \end{bmatrix} \quad (3)$$

Combining Eq. (1) to Eq. (3), we obtain the geometric imaging model of star observation:

$$\begin{bmatrix} \cos\alpha \cdot \cos\delta \\ \sin\alpha \cdot \cos\delta \\ \sin\delta \end{bmatrix} = m \mathbf{R}_{Cam}^{J2000}(t_i) \begin{bmatrix} x-x_0 \\ y-y_0 \\ -f \end{bmatrix} \quad (4)$$

Eq. (4) indicates that the accuracy of the image side coordinates (x, y) and object side coordinates (α, δ) are the key factors of the imaging models. The attitude accuracy of $\mathbf{R}_{Cam}^{J2000}(t_i)$ is also important for the imaging model owing to the different imaging time of each line. These two aspects, namely, the accurate extraction method of SCPs and the geometric calibration model for star observation, need to be dealt with separately.

B. Accurate extraction method of SCPs

1) Image/Object side coordinate extraction of SCPs

The satellite camera is pointed to deep space to capture images, which are originally all-black images except for the stars. However, each pixel within the linear array responds differently and thus has a certain amount of random noise, which is commonly referred to as background noise. After imaging with push broom, the resulting image has a very significant stripe background noise. Therefore, we must first remove it and then obtain the image/object side coordinates of the star.

The digital number (DN) value of each pixel in the star image taken by the linear array camera has a significant trend that gradually decreases or increases from the first line to the last line. The image can be divided into upper and lower parts, and the DN mean values of the corresponding pixel parts can be calculated as follows:

$$\text{StripeNoise}_s = \begin{cases} aa_s = \sum_{l=0}^{h/2} \sum_{s=0}^w DN_{l,s} \times 2/h \\ bb_s = \sum_{l=h/2}^h \sum_{s=0}^w DN_{l,s} \times 2/h \end{cases} \quad (5)$$

where $DN_{l,s}$ represents the pixel DN values at the locations where the line (or row) and sample (or column) are l and s , respectively. h and w represent the image height and width, respectively. aa_s is the mean DN value of the different columns in the upper half of the image, and bb_s is the mean DN value of the different columns in the lower half of the image. StripeNoise_s is the noise of pixel s in the linear array. The estimated value of stripe background noise for each pixel can be obtained by the slope equation, which is derived as follows:

$$\text{PixelNoise}_{l,s} = 2l \times (bb_s - aa_s)/h + (3aa_s - bb_s)/2 \quad (6)$$

Stars usually appear as circular bright spots in an image, and we can extract them from the image by separating them with stripe background noise. The image can be binarized as follows:

$$B_{l,s} = \begin{cases} 1, & DN_{l,s} \geq \text{PixelNoise}_{l,s} + T \\ 0, & DN_{l,s} < \text{PixelNoise}_{l,s} + T \end{cases} \quad (7)$$

T is the extraction threshold, and $B_{l,s}$ is a binary image. We mark the parts with a value of 1 in $B_{l,s}$ using the connected domain algorithm to obtain k sets of connected domains $\Omega_i, i = \{1, 2, \dots, k\}$. Then, each connected domain may be a star. Using the grayscale weighted centroid method to extract the central coordinates of the connected region, the centroid subpixel coordinates (x_i, y_i) of the i -th star can be obtained. The calculation formula is:

$$\begin{cases} x_i = \sum_{(x,y) \in \Omega_i} x \cdot G_{x,y}^2 / \sum_{(x,y) \in \Omega_i} G_{x,y}^2 \\ y_i = \sum_{(x,y) \in \Omega_i} y \cdot G_{x,y}^2 / \sum_{(x,y) \in \Omega_i} G_{x,y}^2 \end{cases} \quad (8)$$

In general, linear array cameras have a narrow field of view, and the stars captured are mainly of higher magnitude (lower brightness). As the magnitude increases, the number of stars increases exponentially. Conventional star identification algorithms cannot easily identify stars captured by linear array cameras. Therefore, the existing satellite attitude information and geometric positioning models for star observation can be used to predict the star positions, and then the stars can be identified. Thus, the SCPs can be represented as follows:

$$\text{SCP} \Rightarrow (x_i, y_i) \equiv (\alpha_i, \delta_i). \quad (9)$$

2) Astronomical coordinate correction of SCPs

Owing to the epoch difference between a star catalog and the star observation time by the satellite, the position of the star in the celestial coordinate system is different. Although the positions of most stars remain unchanged under naked eye observation. When considering the geometric calibration of

> REPLACE THIS LINE WITH YOUR MANUSCRIPT ID NUMBER (DOUBLE-CLICK HERE TO EDIT) <

high-resolution cameras, even small differences can cause errors in parameter solving. Their errors must be corrected. This could be represented by the proper motion parameters in the star catalog. If we assume that the proper motion of a star is constant for a few years, and the epoch difference between the star catalog and the observed time is t years, the correct position of the star is expressed:

$$\alpha_i = \bar{\alpha}_i + \Delta\alpha * t, \delta_i = \bar{\delta}_i + \Delta\delta * t \quad (10)$$

where $\bar{\alpha}_i$ and $\bar{\delta}_i$ represent the star coordinates at the star catalog, and $\Delta\alpha$ and $\Delta\delta$ are the proper motion parameters of the stars at right ascension and declination, respectively. Meanwhile, α_i and δ_i represent the object coordinates of the i -th star at the time of satellite imaging.

Meanwhile, the positions of stars in the star catalog are described by stationary observers. When satellites move around the Earth at high speed, the light aberration of the observing stars cannot be ignored under the effect of Einstein's theory of relativity. The equation for correcting the light aberration is:

$$\beta = \frac{v}{c} \sin\eta \quad (11)$$

where β is the aberration offset angle, v denotes the motion velocity of the satellite in the heliocentric inertial coordinate system. c is the speed of light, and η represents the angle between the satellite motion direction and the camera optical axis direction. The correction process is detailed in [5].

The light aberration correction can also be expressed as the rotation matrix $\mathbf{R}_{Aber}(t_i)$, which depends on β and the imaging time. The star observation model for a linear array camera after accounting for astronomical coordinate correction is:

$$\begin{bmatrix} \cos\alpha \cdot \cos\delta \\ \sin\alpha \cdot \cos\delta \\ \sin\delta \end{bmatrix} = m \mathbf{R}_{Aber}(t_i) \mathbf{R}_{Cam}^{J2000}(t_i) \begin{bmatrix} x - x_0 \\ y - y_0 \\ -f \end{bmatrix} \quad (12)$$

where (α, δ) are the right ascension and declination of the star after proper motion correction.

C. Geometric calibration model of linear array camera for star observation

1) Geometric calibration model and equivalent distortion model

After we obtain the coordinates of the image side (x_i, y_i) and object side (α_i, δ_i) of the i -th star in the camera, we can construct a geometric calibration model of linear array cameras for star observation with Eq. (12):

$$\begin{bmatrix} \cos\alpha_i \cdot \cos\delta_i \\ \sin\alpha_i \cdot \cos\delta_i \\ \sin\delta_i \end{bmatrix} = m_i \mathbf{R}_{Aber}(t_i) \mathbf{R}_{Cam}^{J2000}(t_i) \mathbf{R}\mathbf{u} \begin{bmatrix} x_i - x_0 + \Delta x \\ y_i - y_0 + \Delta y \\ -f \end{bmatrix} \quad (13)$$

where $\mathbf{R}\mathbf{u}$ is the exterior orientation compensation matrix, and $(\Delta x, \Delta y)$ is the interior orientation compensation parameter. $\mathbf{R}\mathbf{u}$ can be represented by the following three Euler angles $(\varphi, \omega, \kappa)$:

$$\mathbf{R}\mathbf{u} = \begin{bmatrix} \cos\varphi & 0 & \sin\varphi \\ 0 & 1 & 0 \\ -\sin\varphi & 0 & \cos\varphi \end{bmatrix} \begin{bmatrix} 1 & 0 & 0 \\ 0 & \cos\omega & -\sin\omega \\ 0 & \sin\omega & \cos\omega \end{bmatrix} \begin{bmatrix} \cos\kappa & -\sin\kappa & 0 \\ \sin\kappa & \cos\kappa & 0 \\ 0 & 0 & 1 \end{bmatrix} \quad (14)$$

$(\Delta x, \Delta y)$ can be represented by the principal point errors $(\Delta x_0, \Delta y_0)$, principal distance errors Δf , radial distortion parameters (k_1, k_2, \dots) , and eccentric distortion parameters (p_1, p_2) :

$$\begin{cases} \Delta x = \Delta x_0 + \frac{x'}{f} \Delta f + (k_1 r^2 + k_2 r^4) \cdot x' + p_1 (r^2 + 2x'^2) + 2p_2 x' y' \\ \Delta y = \Delta y_0 + \frac{y'}{f} \Delta f + (k_1 r^2 + k_2 r^4) \cdot y' + p_2 (r^2 + 2y'^2) + 2p_1 x' y' \end{cases} \quad (15)$$

where $(x', y') = (x_i - x_0, y_i - y_0)$, $r^2 = x'^2 + y'^2$.

Linear array cameras have a constant value C in the direction of x . The higher-order terms of radial distortion for aerospace level cameras can generally be ignored; therefore, the interior orientation element error compensation model is equivalent to:

$$\begin{cases} \Delta x = \Delta x_0 + \frac{C}{f} \Delta f + k_1 (C^2 + y'^2) \cdot C + p_1 [(C^2 + y'^2) + 2C^2] + 2p_2 C y' \\ \Delta y = \Delta y_0 + \frac{y'}{f} \Delta f + k_1 (C^2 + y'^2) \cdot y' + p_2 [(C^2 + y'^2) + 2y'^2] + 2p_1 C y' \end{cases} \quad (16)$$

We can expand Eq. (16), merge the same sub term coefficients, and replace the variables with:

$$\begin{cases} \Delta x = m_0 + m_1 y' + m_2 y'^2 \\ \Delta y = n_0 + n_1 y' + n_2 y'^2 + n_3 y'^3 \end{cases} \quad (17)$$

where:

$$\begin{cases} m_0 = \Delta x_0 + \frac{C}{f} \Delta f + k_1 C^3 + 3p_1 C^2 \\ m_1 = 2p_2 C \\ m_2 = k_1 C + p_1 \\ n_0 = \Delta y_0 + p_2 C^2 \\ n_1 = \frac{1}{f} \Delta f + k_1 C^2 + 2p_1 C \\ n_2 = 3p_2 \\ n_3 = k_1 \end{cases} \quad (18)$$

We can expand Eq. (17) again with $y' = y - y_0$, merge the same secondary coefficient, and replace the variables with:

$$\begin{cases} L(y) = a_0 + a_1 y + a_2 y^2 \\ S(y) = b_0 + b_1 y + b_2 y^2 + b_3 y^3 \end{cases} \quad (19)$$

where $L(y)$ represents a line direction polynomial, and $(a_i, i = 0, 1, 2)$ represents a polynomial coefficient. $S(y)$ represents a sample direction polynomial, and $(b_i, i = 0, 1, 2, 3)$ represents a polynomial coefficient. The number of unknowns is consistent with the distortion model. Therefore, for a linear array camera, the function of line direction distortion is related to sample y with the highest order of 2. The function of sample direction distortion is related to sample y with the highest order of 3. Therefore, the problem of solving the parameters of the

> REPLACE THIS LINE WITH YOUR MANUSCRIPT ID NUMBER (DOUBLE-CLICK HERE TO EDIT) <

nonlinear distortion model is transformed into a linear parameter solving problem, which increases the stability of the solution of the interior calibration.

2) Correction strategies for non-stationary attitude

Stars are in different lines in the image, which means that they have different imaging times and corresponding attitudes. As shown in Fig. 1, star observation requires satellite attitude rotation, which is not a stable imaging process. And the frequency of the attitude measurement (8 Hz) cannot reach the imaging lines per second (almost 1000 Hz). The random errors caused by non-stationary attitude will lead to a decrease in the accuracy of the overall calibration model. Therefore, non-stationary attitude errors cannot be ignored in linear array camera calibration. The ground-based calibration field can match massive ground control points (GCPs) within a short imaging period. The impact of attitude error on calibration can be minimized. However, owing to the sparsity of the star distribution, the SCPs are insufficient when we adopt a short period. Therefore, increasing the SCPs and decreasing the imaging period are conflicting requirements. At this point, the correction of non-stationary attitude becomes a key factor.

After the exterior geometric calibration, the theoretical image side coordinate of the star can be calculated by the object side coordinate based on Eq. (13). Compared with the extracted object side coordinate, the position error is mainly composed of the attitude error and interior parameters error. Different SCPs can compensate each other's interior parameters error. The more SCPs involved in the calibration model, the larger the proportion of the attitude measurement error can be counted. Therefore, the correction strategies for non-stationary attitude are by using the position error to restore attitude error. If the position error of the i -th star is $(\Delta l, \Delta s)$, the attitude correction rotation matrixes across and along the track direction are:

$$\begin{cases} \mathbf{R}_\omega = \begin{bmatrix} 1 & 0 & 0 \\ 0 & \cos\Delta\omega & -\sin\Delta\omega \\ 0 & \sin\Delta\omega & \cos\Delta\omega \end{bmatrix} \\ \mathbf{R}_\varphi = \begin{bmatrix} \cos\Delta\varphi & 0 & \sin\Delta\varphi \\ 0 & 1 & 0 \\ -\sin\Delta\varphi & 0 & \cos\Delta\varphi \end{bmatrix} \end{cases} \quad (20)$$

where

$$\begin{cases} \Delta\omega = \arctan(\Delta s/f) \\ \Delta\varphi = \arctan(\Delta l/f) \end{cases} \quad (21)$$

Then, the attitude correction for the i -th is:

$$\mathbf{R}_{Cam}^{J2000}(t_i)_{fix} = \mathbf{R}_\varphi \mathbf{R}_\omega \mathbf{R}_{Cam}^{J2000}(t_i) \quad (22)$$

Using this corrected attitude for recalibration minimizes the effects of non-stationary attitude errors.

III. DATA

A. Jilin-1 satellite data

In this study, the “Jilin-1” GF03D-03 linear array satellite was used to photograph stars, and its calibration accuracy was verified. Jilin-1 is the world's largest sub-meter commercial remote sensing satellite constellation, with 108 satellites in orbit (until June 2023). GF is the abbreviation of “Gaofen”, which means high resolution in Chinese. The GF03 series comprises third-generation satellites of the Jilin-1 satellite constellation. They are mass-produced satellites with low cost, low power consumption, and a weight of 43 kg. GF03D is the latest type in this series, with 44 satellites currently in orbit (until June 2023). The GF03D linear array satellite consists of three linear array charge coupled devices (CCDs), with a resolution of 1 m for subsatellite points and a width exceeding 17 km. This study used the third satellite of the GF03D series for experiments.

TABLE I
TECHNICAL SPECIFICATIONS OF THE “JILIN-1” GF03D-03 SATELLITE

Overall situation	Total mass	43 kg
	Launch date	July 3rd, 2021
	Imaging mode	Ground observation, Deep space bserveation
Orbit	Orbit type	Sun synchronous
	Orbit height	535 km
Attitude	Measurement style	Dual star trackers and three-axis gyroscope
	Measurement frequency	8 Hz
	Pixel size	6150 pixels × 3 CCD
Camera	Ground imaging width	> 17 km
	Ground resolution	1 m
	Field of view	2°
Camera	Pixel angle resolution	0.38"
	Pixel quantization	12bit
	Maximum TDI level	96

This experiment uses data from four tasks acquired by the Jilin-1 GF03D-03 satellite. Two of them are star observation data and two are ground observation data (see Table II). The Pleiades cluster was observed in two star images (Task S01 and S02), and the Jilin province and Chongqing City in China were photographed in two ground images (Task G01 and G02). Owing to the increase in the linear array exposure time, obtaining a star image takes longer with the same standard scene size. As shown in Table II, the observation time for S01 is 20 s, while the observation time for G01 is only 2.4 s.

TABLE II
BASIC SITUATION OF THE STAR AND GROUND OBSERVATION DATA

> REPLACE THIS LINE WITH YOUR MANUSCRIPT ID NUMBER (DOUBLE-CLICK HERE TO EDIT) <

Task ID	Observation time	Observation target	Exposure time per line	Imaging duration	Imaging range (reference coordinate system)	Image size
S01	2023.01.11	Pleiades Cluster	1.07 ms	20s	55.7°~58.1°, 22.8°~25.2° (J2000)	18450*17800
S02	2023.02.10	Pleiades Cluster	1.07 ms	40s	55.6°~57.8°, 22.8°~26.6° (J2000)	18450*36000
G01	2023.01.15	Jilin, China	0.14 ms	2.4s	123.4°~123.7°, 43.7°~43.9° (WGS84)	18450*17800
G02	2023.01.29	Chongqing, China	0.14 ms	2.4s	105.5°~105.8°, 30.2°~30.4°(WGS84)	18450*17800

B. Star catalog data

For this experiment, we used the GAIA EDR2 catalog, published in April 2018, which contains measured parameters for 1.69 billion celestial bodies [20]. The original GAIA catalog data contain stars up to magnitude 21, with a data volume of approximately 1.26 TB. The “Jilin-1” GF03D satellite series can photograph stars of magnitude 12. In this catalog, there are approximately 1.24 million stars under magnitude 12. Considering the accuracy, stars with magnitudes less than 10.5 in the GAIA catalog are selected as SCPs.

This experiment focuses on observing the Pleiades cluster, considering mainly the following factors. The Pleiades is an open star cluster in the Taurus constellation. The field of view of the Pleiades cluster is approximately 2°, covering the entire

field of view of the linear array camera. There are many stars with magnitudes between 7 and 9, which appear as relatively small star points in the image, and the extraction accuracy of the star coordinates is higher. Therefore, the Pleiades cluster is very suitable for camera calibration, especially for interior calibration. Because most of the stars in the Pleiades cluster are only 400 light years away from Earth, their proper motions are relatively obvious. As shown in Table III, most stars in the Pleiades cluster have a relatively uniform direction of proper motion in right ascension (Pmra) and declination (Pmde). However, some stars have nonuniform directions of proper motion (such as the star of magnitude 6.85). The proper motion unit is milliarcseconds per year (mas/yr). In the case of precise interior calibration, we must accurately correct for the influence of the proper motion of the star.

TABLE III
OVERVIEW OF THE STAR CATALOG PARAMETERS

GAIA star catalog ID	Right ascension and declination (deg, J2015.5 epoch)		Pmra and Pmde (mas/yr)		Magnitude
66714384141781760	56.87124°	24.10494°	25.3	-45.9	2.77
65283232318680704	56.45679°	24.36754°	19.3	-44.5	3.81
65205373151673344	56.58166°	23.94815°	15.3	-49.9	4.09
65010690873940480	56.82126°	23.72663°	-34.1	-26.4	6.85
65008698009126528	56.64258°	23.62382°	24.9	-44.0	8.03
66802654309459712	56.41749°	24.62703°	18.1	-43.8	9.59

IV. EXPERIMENT

A. Star image denoising effect

First, the stars with stripe background noise need to be filtered out from the original image. On the left of Fig. 3 shows the original star observation image and its horizontal/vertical profile value. The values of the horizontal profile show that the stripe background noise in the image is obvious. The area A and area B are chosen as examples. A1 is the enlarged view of area A which has 3 stars with magnitude of 6.28, 8.23 and 8.6. B1 is the enlarged image of area B which has 1 star with magnitude of 5.57. The corresponding background noise image (A2 and

B2) and binarization image (A3 and B3) are shown on the right side of Fig. 3. The horizontal profiles are corresponding to the image above and each cross a star. From the horizontal profile, the background noise calculated by equation (5) and (6) in this study can effectively separate stars. These two examples respectively demonstrate the extraction of star points in areas with abrupt changes in stripe background noise, as well as the extraction of different magnitudes of stars from background noise. Through the stripe background noise removal method in this study, all stars (magnitude below 10.5) can be well distinguished from background noise regardless of where they appear in the image. More typical star extraction results can be found in the next section on SCPs extraction results.

> REPLACE THIS LINE WITH YOUR MANUSCRIPT ID NUMBER (DOUBLE-CLICK HERE TO EDIT) <

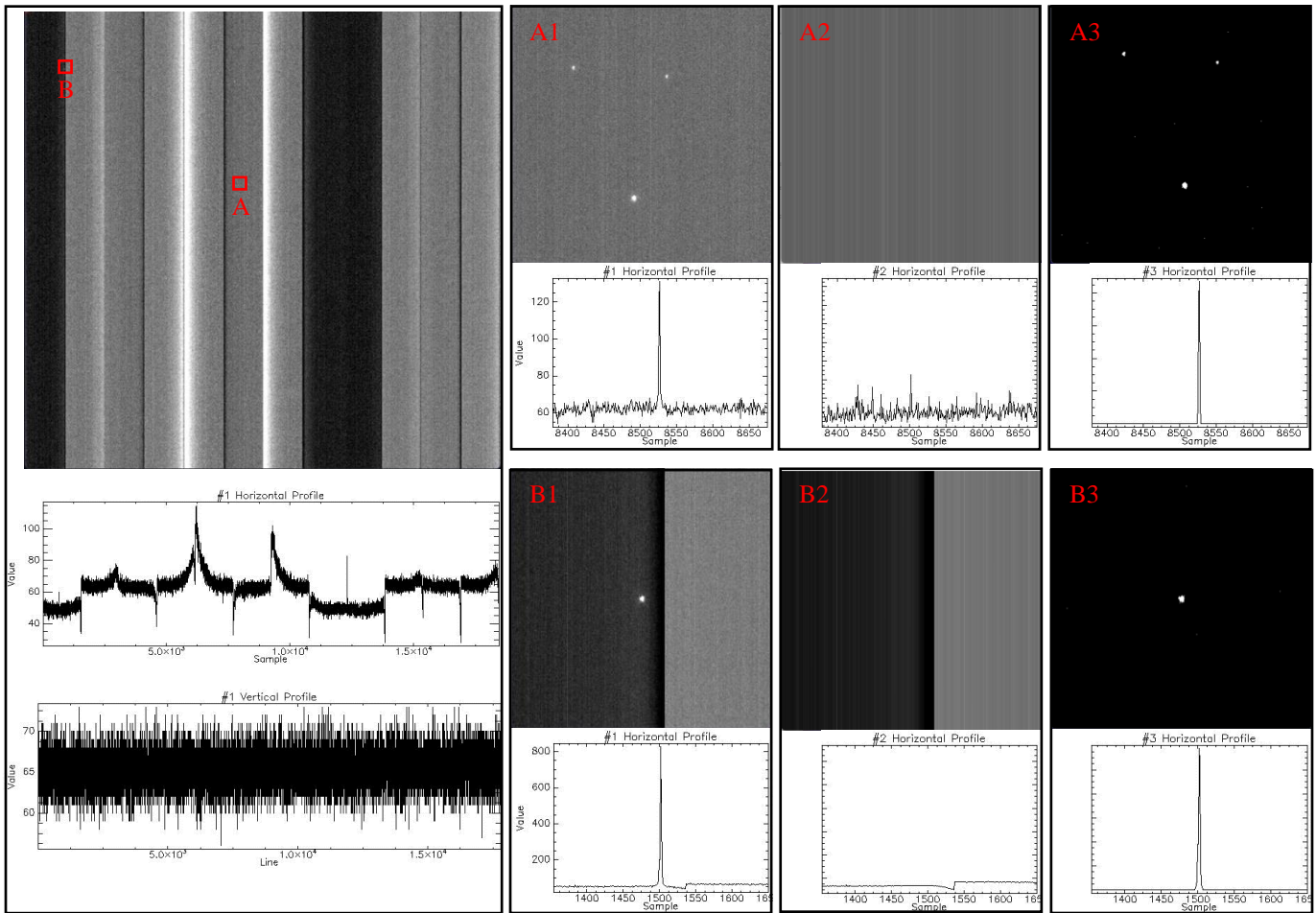


Fig. 3. The star observation image taken by linear array camera and its profile value (left: original star observation image and its profile value across area A; A1 and B1: enlarged image of area A and B, respectively; A2 and B2: corresponding background noise; A3 and B3: corresponding binarization image after denoising)

B. SCPs extraction results

Fig. 4 and Fig. 5 show the results of star point extraction and identification from two observation experiments, S01 and S02. The coordinate systems in both figures are drawn in the north-south direction according to the celestial coordinate system. The push broom direction in Fig. 4 is from top left to bottom right, while Fig. 5 is from top to bottom. The imaging time of Fig. 4 is only half of that of Fig. 5, so the image is only half the length of Figure 5. This demonstrates the freedom of imaging attitude and has fewer limitations in star observation modes.

In Fig. 4 and Fig. 5, the black solid circle is a star simulated by the GAIA catalog. The larger the area of a solid circle, the brighter the star. The stars extracted from the image are shown as red circles. Stars identified from the image are shown as blue boxes in the image. Some parts of the red circle are not stars but are the effect of noise and cosmic rays. In this experiment, only stars with magnitudes less than 10.5 are chosen and the stars identified by blue boxes are used as SCPs. Finally, Fig. 4 includes 73 SCPs, while Fig. 5 includes 100 SCPs as the observation time was longer.

Table IV shows the image/object side coordinate and magnitudes of several typical SCPs extracted from S01. The

morphology of the stars in the image and the horizontal/vertical DN value distribution of the stars are also given.

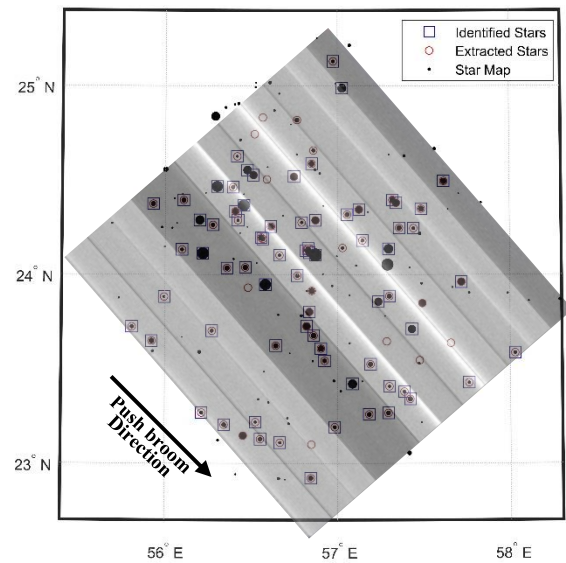


Fig. 4. Extraction and identification results of S01 (The background is a semitransparent star observation image)

> REPLACE THIS LINE WITH YOUR MANUSCRIPT ID NUMBER (DOUBLE-CLICK HERE TO EDIT) <

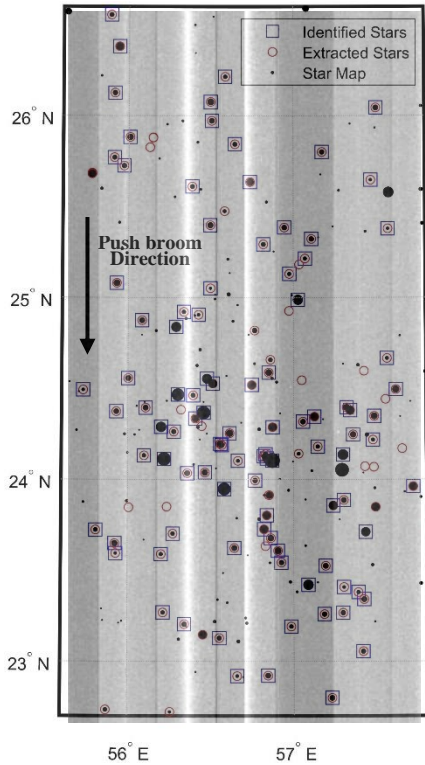
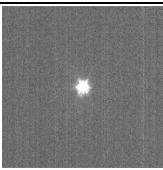
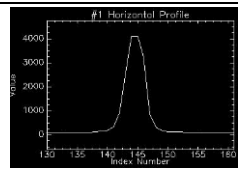
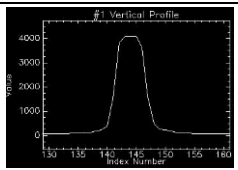

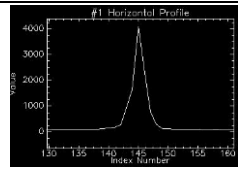
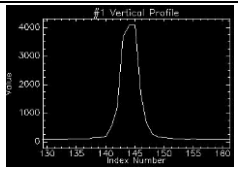
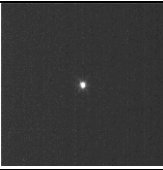
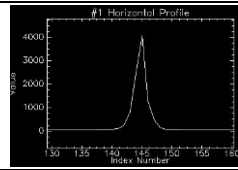
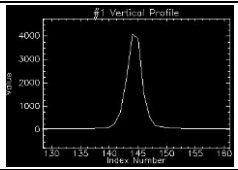
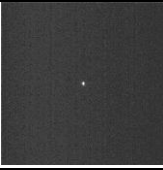
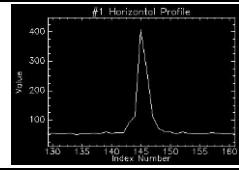
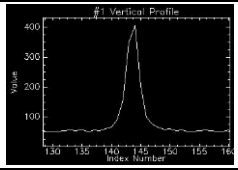


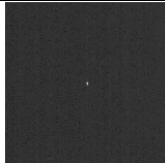
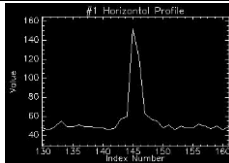
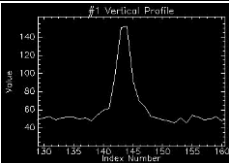
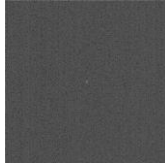
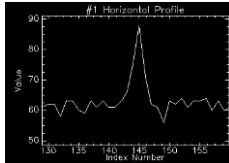
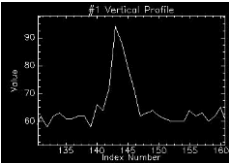
Fig. 5. Extraction and identification results of S02 (The background is a semitransparent star observation image)

Stars with low magnitude, i.e., high brightness, do not appear close to a circle, which affects the accuracy of the star point centroid extraction. For example, the typical stars in the Pleiades cluster are Alcyone, Maia, and Merope (Table IV No.1,2,3). Theoretically, the star brightness curve follows a Gaussian distribution. When the magnitude is approximately below 5, some stars may be overexposed. This phenomenon results in a value of 4095, the brightness curve cannot accurately describe the energy distribution of the star, and the accuracy of the star point extraction decreases. Therefore, during the calibration process, the weights of high-brightness SCPs in the model are reduced accordingly. As shown in Table IV, No.4, when the magnitude is approximately 6.85, the DN value in the linear array image is approximately 400. At this point, stars and background noise can be well distinguished. As the star magnitude becomes larger, the conventional star catalog (such as the HIP star catalog) can no longer record these stars. But the GAIA catalog fully records the positions and other information of these stars (Table IV, No.5,6). As shown in the distribution curve of the DN values, the brightness and background noise of low-brightness stars are relatively close (Table IV, No.6). Therefore, during the calibration process, the weights of low-brightness stars in the calibration model are also reduced accordingly. The above measures improve the accuracy of interior orientation element calculation in the calibration model.

TABLE IV
OVERVIEW OF SCPs IN S01 STAR OBSERVATION IMAGES

No. (name)	SCP (star control point)			Star image	Horizontal DN value distribution	Vertical DN value distribution
	Pixel position	Object position (J2015.5 epoch)	Magn- itude			
1 (Alcyone)	$x=7729.44$ $y=8322.22$	$\bar{\alpha}=56.87124^\circ$ $\bar{\delta}=24.10494^\circ$	2.77			
2 (Maia)	$x=3585.61$ $y=9461.55$	$\bar{\alpha}=56.45679^\circ$ $\bar{\delta}=24.36754^\circ$	3.81			
3 (Merope)	$x=7267.85$ $y=11213.27$	$\bar{\alpha}=56.58166^\circ$ $\bar{\delta}=23.94815^\circ$	4.09			
4 (HIP 17684)	$x=10165.16$ $y=10976.99$	$\bar{\alpha}=56.82126^\circ$ $\bar{\delta}=23.72663^\circ$	6.85			

> REPLACE THIS LINE WITH YOUR MANUSCRIPT ID NUMBER (DOUBLE-CLICK HERE TO EDIT) <

5 (GAIA ID: 650086980 09126528)	$x=9923.08$ $y=13185.90$	$\bar{\alpha}=56.64258^\circ$ $\bar{\delta}=23.62382^\circ$	8.03			
6 (GAIA ID: 668026543 09459712)	$x=1517.40$ $y=8123.22$	$\bar{\alpha}=56.41749^\circ$ $\bar{\delta}=24.62703^\circ$	9.59			

V. DISCUSSION

To verify the accuracy of the calibration parameters obtained from the star observation, this experiment is discussed step by step from four points of view, as shown in Fig. 6. Firstly, the self-verification experiment is performed. Star image 01 (S01) is both a calibration scene and a verification scene. This experiment mainly verifies the accuracy that can be achieved by the star observation model and processing. Secondly, the calibration parameters obtained from S01 are used to verify star

image 02 (S02). This experiment is mainly used to verify the stability of the star-based calibration methods and parameters. Thirdly, the calibration parameters obtained from S01 are used to verify ground image 01 (G01) and ground image 02 (G02). This verifies that the calibration parameters of the stars can also be used for the ground image. Fourthly, adopting the calibration parameters of S01 and G01 and using the G02 for verification, we compare the differences between the parameters obtained from the star observation and ground observation. And the time efficiency of star- and ground-based calibration is compared.

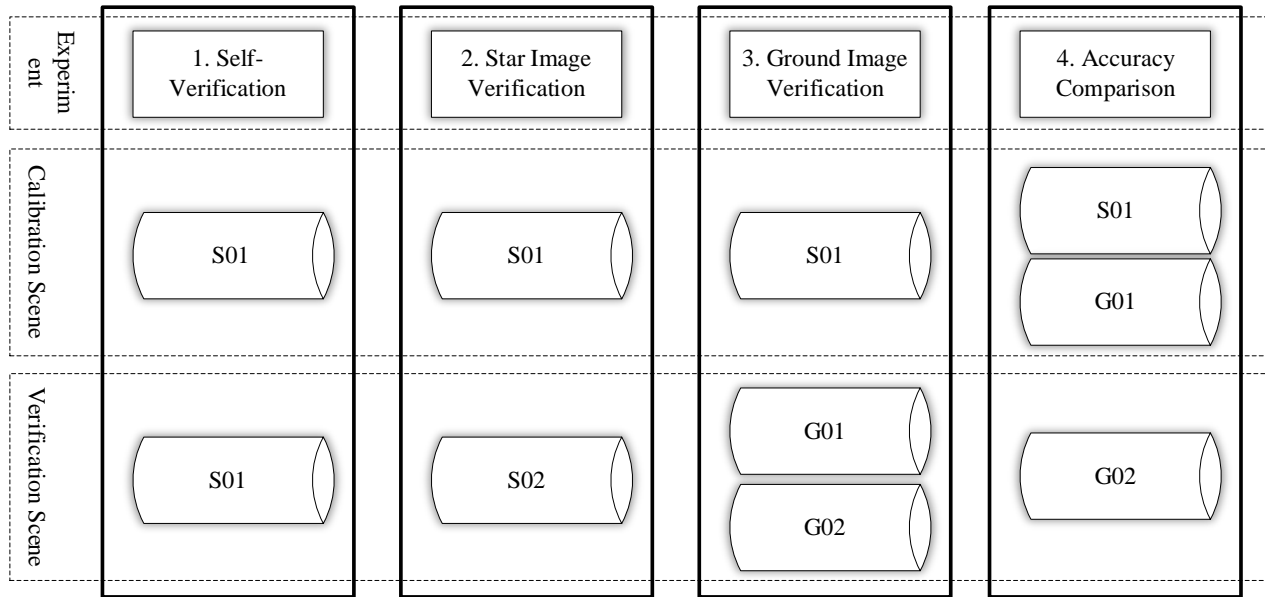


Fig. 6. Correspondence between calibration and validation scenarios for the four validation experiments

A. Self-verification of star-based calibration accuracy

The calibration parameters acquired from S01 were used in S01 to verify the calibration accuracy of each method after processing, and the results are listed in Table V. In the initial condition, 73 SCPs were used as check points (CPs) to verify the geometric positioning accuracy of the image. The plane accuracy was very low, reaching 3910 pixels, which is mainly due to errors in the line direction. After the exterior calibration (EC), the positioning accuracy was effectively improved. After verification with 73 CPs, the accuracy reached 9.048 pixels. After the interior calibration (IC), most of the distortions were effectively eliminated, with an accuracy of 1.179 pixels. After the attitude correction (AC) for the attitude measurement error,

the accuracy of the geometric calibration reached 0.508 pixel. After accounting for the astronomical coordinates correction (CC) of the stars, the calibration accuracy reached 0.287 pixel.

We obtained the error distribution using different methods (see Fig. 7). After EC, the maximum error of the star before processing is approximately 28 pixels. In Fig. 7(a), the red diamonds represent the residual of the star coordinates in the sample direction after the EC, and the green square represents the residual after EC+IC. The red curved shape represents the distortion of the camera in the sample direction. It is evident that EC alone cannot eliminate the distortion of the camera. After IC, the overall error tends to be flat. However, the residual error remains large and needs further correction. In Fig. 7(b), the green squares represent the residual error of the star

> REPLACE THIS LINE WITH YOUR MANUSCRIPT ID NUMBER (DOUBLE-CLICK HERE TO EDIT) <

coordinates in the sample direction after EC+IC (these data are used as reference data in this case). The yellow circle further

decreases the residual error after AC, whose effect is clear. The blue triangles represent the residual error after further CC.

TABLE V
VALIDATION STATISTICS FOR CALIBRATION PARAMETER ACCURACY OF STAR IMAGE S01

Method	No. SCPs/CPs	Sample (pixels)			Line (pixels)			Plane RMSE (pixels)
		MIN	MAX	RMSE	MIN	MAX	RMSE	
Initial	0/73	2.474	47.985	35.012	3875.362	3935.094	3910.493	3910.649
EC	73/0	-0.009	-28.330	8.786	-0.052	-6.070	2.161	9.048
EC+IC	73/0	0.002	-2.168	1.098	-0.005	1.293	0.431	1.179
EC+IC+AC	73/0	-0.001	-1.215	0.300	0.006	1.263	0.410	0.508
EC+IC+AC+CC	73/0	0.006	-0.563	0.210	-0.003	-0.563	0.196	0.287

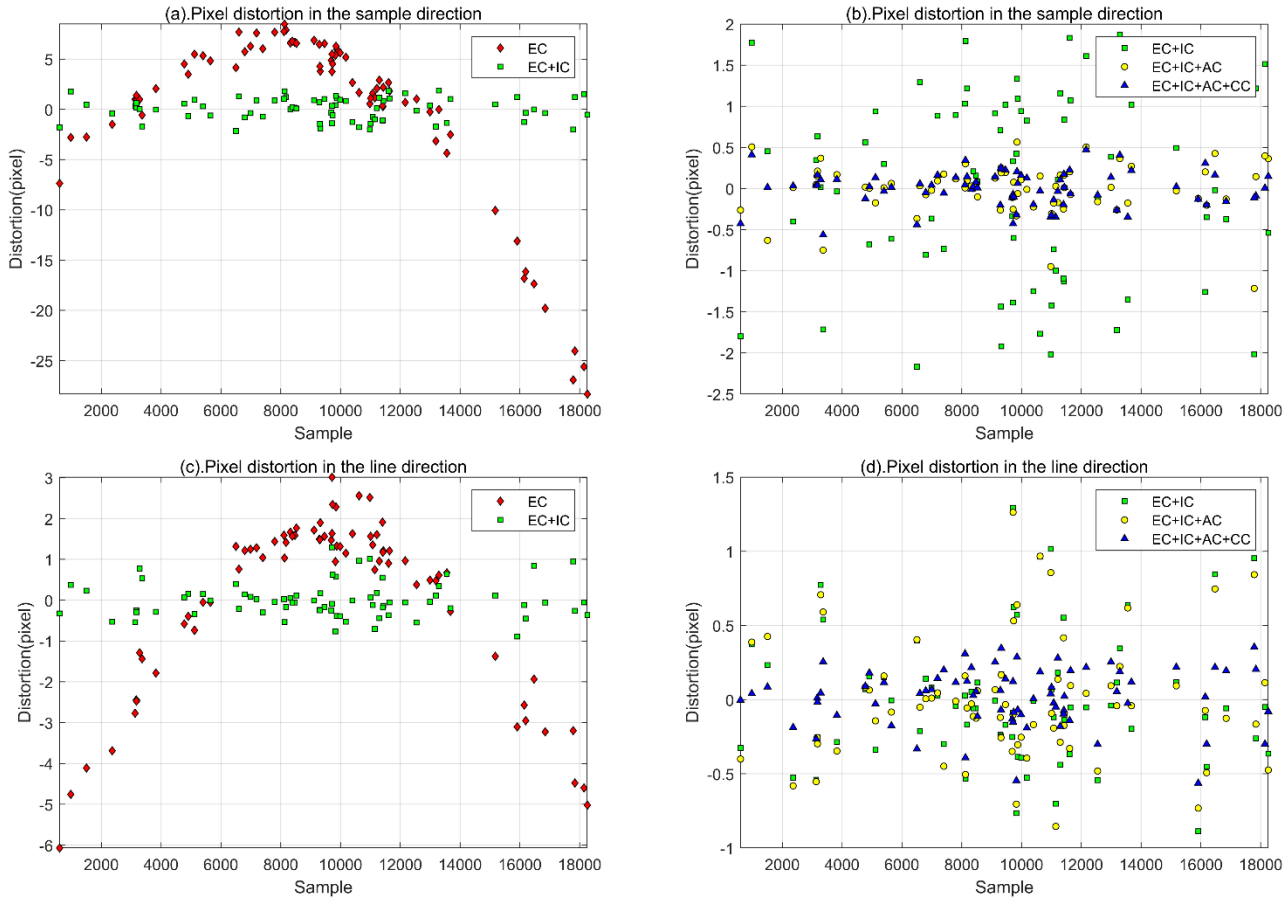


Fig. 7. Schematic diagram of the errors of different processing results for star image S01 (EC: exterior calibration, IC: interior calibration, AC: attitude correction, CC: astronomical coordinate correction)

In Fig. 7(c), the red diamonds represent the residual error of the star coordinates in the line direction after the EC, and the green squares represent the residual error after the EC+IC. The red curved shape represents the distortion of the camera in the line direction. In Fig. 7(d), the yellow circle further increases the residual error after AC. The blue triangles represent the residual error after further CC, whose effect is clear. As can be seen from the catalog parameters in Table III, the proper motion direction of most of the stars in the Pleiades cluster coincides with the pushing direction of the satellite; thus, the correction for the proper motion of stars in the line direction is much more obvious than in the sample. Approximately one-third of the stars move in other directions, so the use of EC parameters cannot compensate for this error. This process also reflects that

the accuracy of SCPs extraction is at least better than 0.3 pixels. If the accuracy of SCPs extraction is lower, the improvement after AC and CC will not be achieved.

In summary, the calibration method described in this study has been subjected to a self-test and can effectively eliminate interior orientation distortion errors of the camera. The accuracy of the S01 interior calibration was better than 0.3 pixel, and the interior accuracy satisfied the needs of most image post-processing and applications.

B. Interior accuracy verification using the star image

Table VI and Fig. 8 illustrate the accuracy verification of the initial parameters and S01 calibration parameters using S02. When there are no control points for the initial parameters, 100

> REPLACE THIS LINE WITH YOUR MANUSCRIPT ID NUMBER (DOUBLE-CLICK HERE TO EDIT) <

SCPs are used as CPs for accuracy verification, and the geometric positioning accuracy is only 3898 pixels. After calibration using 4 SCPs, the geometric positioning accuracy reaches 13.456 pixels. If all 100 SCPs in S02 are used for exterior calibration and the initial interior orientation parameters are adopted, the geometric accuracy improves to 11.938 pixels. The image S02 also exhibits significant distortions. With the calibration parameters of S01, 100 CPs are used for accuracy verification, with a geometric positioning accuracy of 20.102 pixels. This accuracy reflects the geometric positioning accuracy of the Jilin-1 GF03D-03 satellite without control points. The 4 SCPs of S02 are used for exterior

calibration and the interior orientation parameters acquired by S01 are adopted. Then, by verifying 96 CPs in scene S02, the geometric positioning accuracy is 0.597 pixels. If all 100 SCPs in S02 are used for exterior calibration and the interior orientation parameters captured by S01 are adopted, then by verifying all 100 CPs in S02, the geometric positioning accuracy is 0.578 pixels. The accuracy difference between the 4-control and all-control approaches is not significant, which suggests that the interior orientation parameters obtained by the S01 scene can already effectively correct the interior distortion of the image.

TABLE VI
VALIDATION ACCURACY STATISTICS OF THE INITIAL AND S01 CALIBRATION PARAMETERS FOR STAR IMAGE S02

Method	No. SCPs/CPs	Sample (pixels)			Line (pixels)			Plane RMSE (pixels)
		MIN	MAX	RMSE	MIN	MAX	RMSE	
Initial parameters	0/100	-0.042	-30.923	10.910	3866.320	3927.850	3898.158	3898.173
	4/96	-0.030	-26.932	11.967	-0.002	-13.166	6.153	13.456
	100/0	0.131	-31.833	10.928	-0.123	-12.510	4.806	11.938
S01 parameters (EC+IC+AC+CC)	0/100	-9.973	-12.532	11.455	-15.664	-17.469	16.488	20.077
	4/96	-0.002	1.102	0.493	-0.000	0.888	0.338	0.597
	100/0	0.004	0.986	0.479	-0.002	-0.800	0.323	0.578

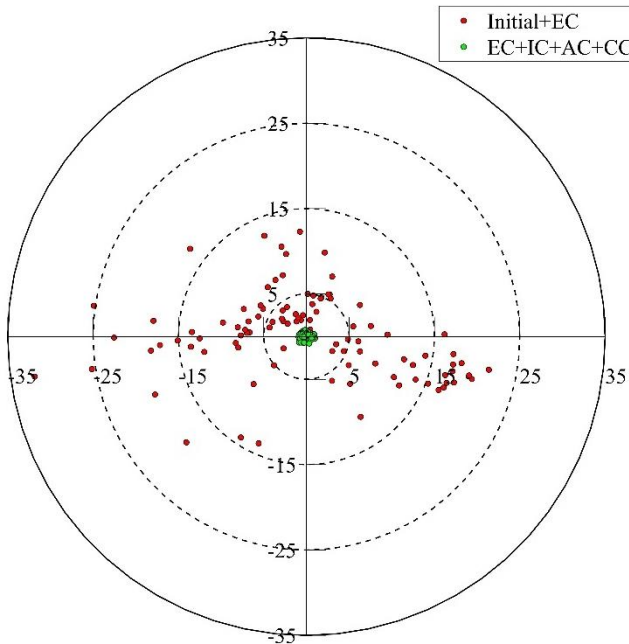


Fig. 8. Schematic diagram of the accuracy verification of the initial and S01 calibration parameters for the star image S02

The error distribution of SCPs before (initial interior parameters + EC) and after (EC+IC+AC+CC) processing is shown in Fig. 8. The maximum error is approximately 31 pixels before processing. After correction, the error distribution is clearly concentrated, with a maximum error of no more than 1 pixel. After the verification of the star images, star-based calibration can accurately restore the interior distortion of the camera. In a sense, star observation can be used not only for calibration, but also for evaluating changes in geometric

accuracy and monitoring the long-term geometric performance of remote sensing cameras. Moreover, this process only requires a small amount of computing resources and can be automated. When constructing the geometric model of S02 by using the parameters of S01, it took less than 5 seconds to predict and extract the SCPs from S02.

C. Interior accuracy verification using the ground image

As shown in Table VII, Fig. 9, and Fig. 10. The accuracy of using S01 parameters and the initial parameters is verified with G01 and G02, respectively.

As shown in Fig. 9, the error directions of the three CCDs can be determined based on the distribution of the arrows when G01 uses the initial interior orientation parameters of the satellite for accuracy verification. Each arrow in Fig. 9 is a ground CPs. These CPs are also GCPs obtained by registration between the ground image and reference image. The error on the right side of CCD3 is the largest. Owing to camera distortions, many CPs errors can exceed 20 pixels. As shown in Table VII, the geometric positioning accuracy without control points reached 4 km using the initial parameters. This is mainly due to the installation errors in the along-track direction. Using 4 GCPs reduced the geometric positioning accuracy to 11.398 m. Using all 5228 GCPs maintained the geometric positioning accuracy to 10.067 m. This indicates that there is a large distortion in the interior orientation of the camera. The MIN/MAX/RMSE errors are similar to those of the star image verification. After using the exterior and interior orientation parameters obtained from S01, we achieved a geometric positioning accuracy of G01 of 20.453 m without control points. Using 4-GCPs decreased the geometric positioning accuracy to 1.481 m. After using all 5228 GCPs, we achieved a geometric positioning accuracy of 1.4 m. Because the GCPs need to be generated at equal intervals within a scene area to better verify the

> REPLACE THIS LINE WITH YOUR MANUSCRIPT ID NUMBER (DOUBLE-CLICK HERE TO EDIT) <

distortions of image, the registration accuracy of some GCPs may be as low as 1 pixel. Therefore, the overall verification accuracy is not within one pixel. Regardless of whether 4 GCPs

or all GCPs are used, the geometric positioning accuracy is basically the same. Most of the geometric positioning residuals of the image have been eliminated.

TABLE VII
G01 AND G02 ERROR DISTRIBUTION STATISTICS BEFORE AND AFTER CALIBRATION OF THE S01 PARAMETERS

Image	Method	No. GCPs/CPs	Across track (meters)			Along track (meters)			Plane RMSE (meters)
			MIN	MAX	RMSE	MIN	MAX	RMSE	
G01	Initial parameters	0/5228	16.520	55.864	46.186	3974.015	4018.401	4002.885	4003.152
		4/5224	-0.002	-22.801	10.929	0.003	7.307	3.235	11.398
		5228/0	-0.005	-27.893	9.673	-0.001	-7.333	2.788	10.067
	S01 parameters (EC+IC+AC+CC)	0/5228	4.253	10.080	7.690	15.395	23.176	18.952	20.453
		4/5224	0.000	-3.762	0.933	0.001	3.379	1.150	1.481
		5228/0	0.000	-3.435	0.874	-0.001	-3.203	1.094	1.400
G02	Initial parameters	0/4255	10.490	47.456	38.580	3975.893	4041.810	4020.089	4020.275
		4/4251	-0.015	-21.486	10.099	-0.001	6.606	3.124	10.571
		4255/0	-0.007	-27.832	7.863	0.001	-6.678	2.278	8.187
	S01 parameters (EC+IC+AC+CC)	0/4255	-0.000	3.172	1.275	29.401	34.907	31.753	31.778
		4/4251	-0.000	-3.791	1.077	0.000	2.876	0.848	1.371
		4255/0	-0.003	-3.753	1.076	0.000	-2.162	0.583	1.224

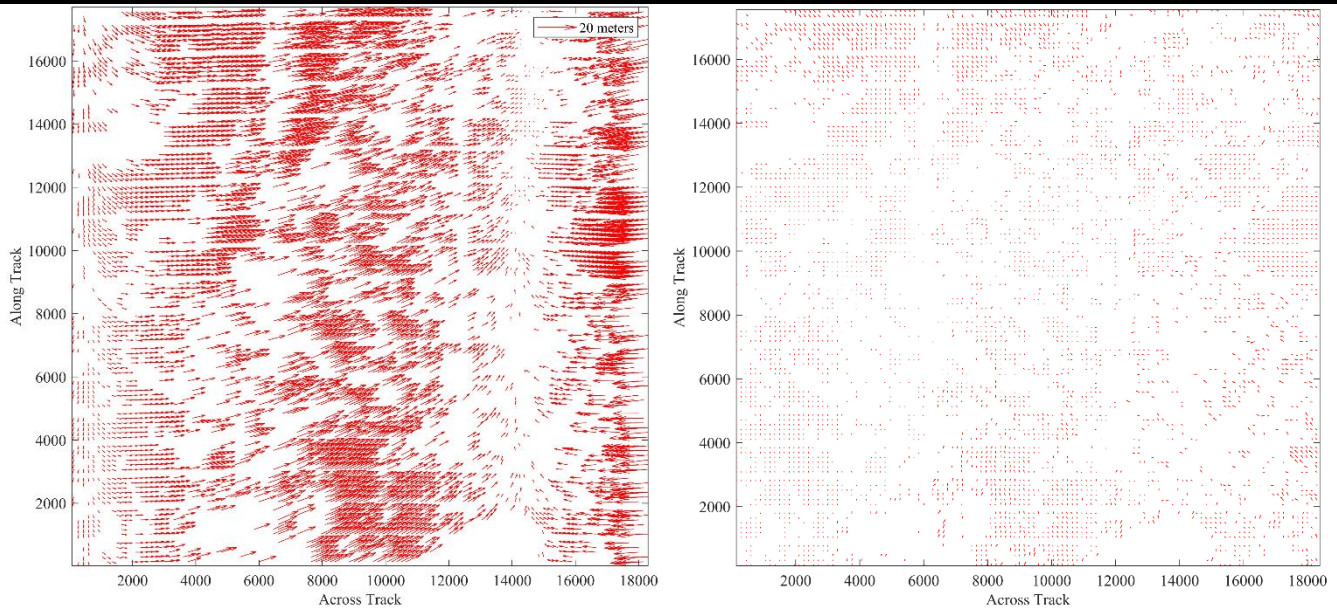


Fig. 9. Error distribution of G01 before and after calibration of S01 parameters

> REPLACE THIS LINE WITH YOUR MANUSCRIPT ID NUMBER (DOUBLE-CLICK HERE TO EDIT) <

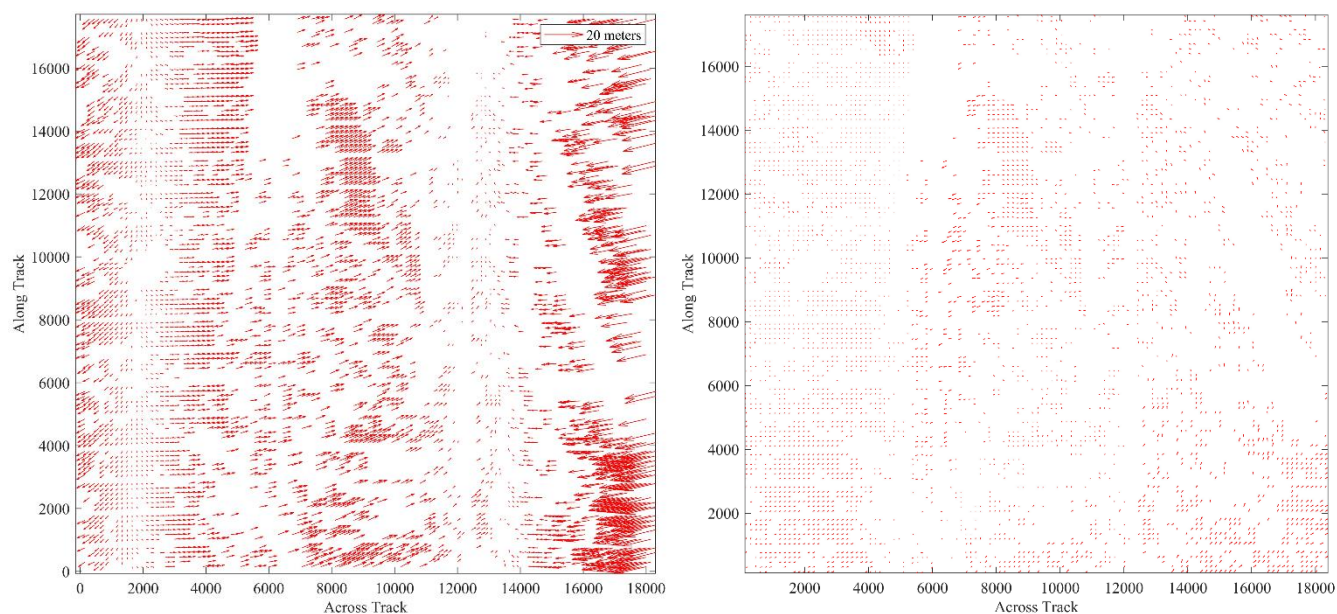


Fig. 10. Error distribution of G02 before and after calibration of S01 parameters

As shown in Fig. 10, the error distribution for G02 is also wide, which uses the initial interior orientation parameters. After statistics, the accuracy of geometric positioning is also 4 km without control points, as listed in Table VII. For 4-GCPs, the geometric positioning accuracy decreased to 10.571 m. For all 4255 GCPs, the geometric positioning accuracy was still only 8.187 m. After using the interior orientation parameters obtained from S01, we achieved a geometric positioning accuracy without control points of 31.778 m. For 4 GCPs, the geometric positioning accuracy decreased to 1.371 m. For all 4255 GCPs, the geometric positioning accuracy was 1.224 m. According to the evaluation results, the geometric positioning accuracy without control points of scene G02 is worse than that of scene G01. The interior accuracy of scene G02 exceeded that of G01. However, this only shows that the GCPs obtained by registration of G02 are more accurate. Because the geometric positioning accuracy is almost the same regardless of whether we use 4 GCPs or all GCPs for G02.

The data in Table VII, Fig. 9, and Fig. 10 indicate that the geometric calibration method of star observation can accurately determine the exterior and interior orientation parameters of the camera. According to the geometric calibration of the Jilin-1 GF03D-03 satellite using SCPs, the accuracy without control points can reach 30 m, and the interior accuracy can reach 1.5 m.

The stitching accuracy of ground images and reference images can be verified using ground products with a

checkerboard method. Take an area from the three CCDs of G01 to display, as shown in Figs. 11–13. On the left sides of Figs. 11–13, only the exterior calibration of G01 is performed using the initial interior orientation parameters. On the right sides of Figs. 11–13, G01 is processed using the S01 interior orientation parameters. The reference maps are overlaid. There is a large deviation between G01 and the reference image when the initial parameters are used. In the checkerboard pattern, the offset direction of CCD1 is on the lower right, the offset direction of CCD2 is on the upper left, and the offset direction of CCD3 is on the right. Owing to the camera distortion, which reaches an error of almost 30 pixels in the edge field of view of CCD3, the deviation of the CCD3 images is very large when adopting the initial parameters. After processing using the star-based calibration parameters of S01, the black and white blocks of the checkerboard are very well aligned. The remaining small offset is mainly caused by the following factors. First, there is a difference in the observation date and angle between the G01 image and the reference image. These two overlapping images have parallax, which is noticeable on objects with some height. Second, no strict radiance correction was applied to G01, and the radiance brightness of the two images was inconsistent, resulting in changes in the road width. Finally, the measurement errors, such as residual errors after attitude correction, lead to small pixel shifts.

> REPLACE THIS LINE WITH YOUR MANUSCRIPT ID NUMBER (DOUBLE-CLICK HERE TO EDIT) <

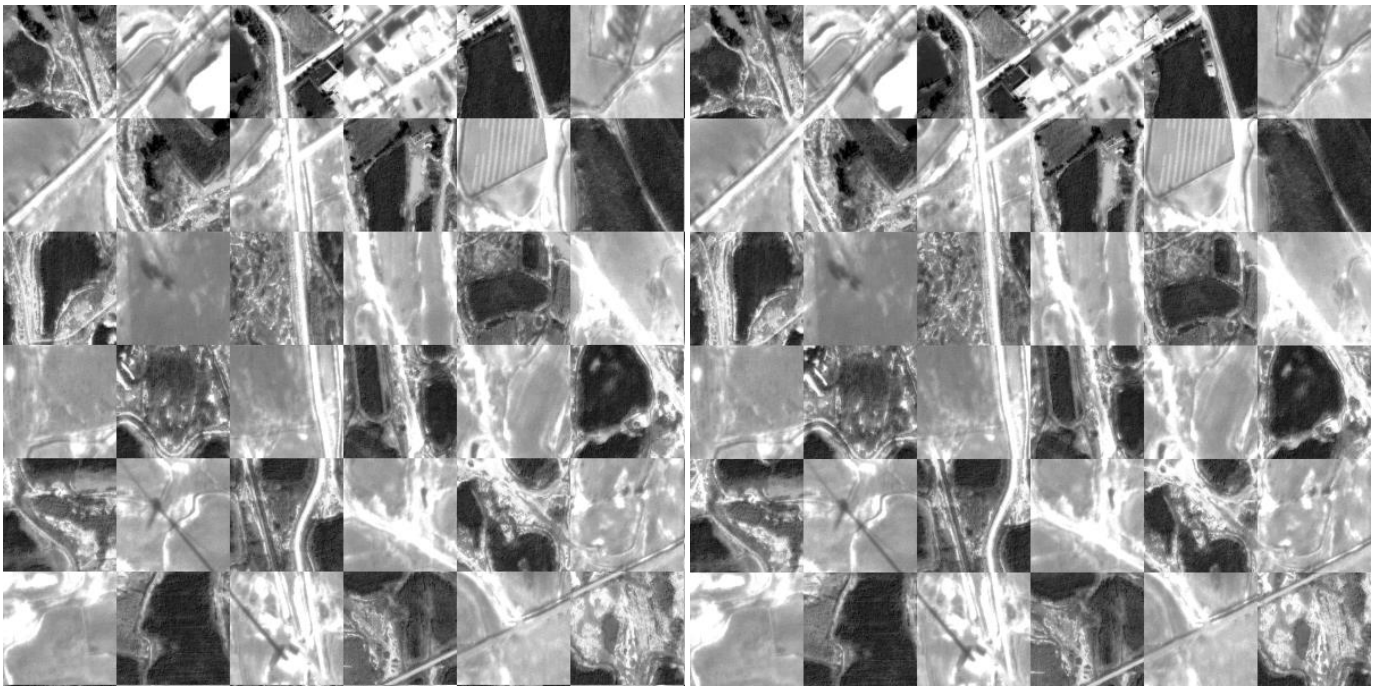


Fig. 11. Comparison of checkerboard patterns of CCD1 image products in G01 before and after S01 parameters processing



Fig. 12. Comparison of checkerboard patterns of CCD2 image products in G01 before and after S01 parameters processing

> REPLACE THIS LINE WITH YOUR MANUSCRIPT ID NUMBER (DOUBLE-CLICK HERE TO EDIT) <



Fig. 13. Comparison of checkerboard patterns of CCD3 image products in G01 before and after S01 parameters processing

D. Comparison of star- and ground-based calibration

In this section, the star-based and ground-based calibration accuracies are first compared. The calibration parameters generated by S01 and G01 are used to verify the accuracy of G02.

As can be seen from Fig. 14, the error distribution of G02, which uses the parameters of S01 for accuracy verification, peaks at 0.6 m and then gradually decreases. According to Table VIII statistics, the maximum error is -3.753 m in the across-track direction and -2.162 m in the along-track direction. The mean square errors in the across- and along-track directions are 1.076 and 0.583 m, respectively. When G02 uses the parameters of G01 for accuracy verification, the error is broadly scattered between 0.7 and 1.1 in the right of Fig.14. The maximum error is 3.116 m in the across-track and 1.731 m in the along-track directions. The mean square errors in the across- and along-track directions are 0.988 and 0.642 m, respectively. The residual distribution between the two is not the same because of the registration error of the verification CPs. The exterior orientation parameters obtained through G01 and S01 are 31.778 m and 30.993 m, respectively. When using the interior orientation parameters of G01 and S01, the statistical results of the plane errors are 1.224 m and 1.178 m, respectively. The geometric positioning accuracy of G02 by using parameters from G01 or S01 are essentially equivalent. This shows that the SCP can completely replace the GCP when it is used.

Next, the time efficiency of star- and ground-based calibration can be compared. The star-based calibration processing time is mainly focused on background noise calculation and connected domain algorithm. For the S01 image in this experiment, these processes take almost 1 minute. After constructing a geometric positioning model for star observation, the interior and exterior calibration can be completed within a few seconds. Considering the reading and writing of images and intermediate data files,

the entire processing time of star-based calibration for an 18450*17800 image takes 90 seconds. In engineering, we can use the historical calibration parameters to predict the position of stars, so that we do not have to read and write the entire image. Then, the calibration time can be shortened to a few seconds. More importantly, due to the robustness and convenience of star identification, this process is automated.

The ground-based calibration processing time are mainly determined by the matching time of the GCPs. Although only a short period of image is required to extract GCPs, such as an 18450*1000 image. The matching time is almost 5 minutes each time. And we need to match at least 3 times to increase the reliability of GCPs. The process of selecting short period of image requires continuous experiment due to ground features change and cloud cover. The entire processing time of ground-based calibration takes at least 20 minutes, and it can only be done manually. Even with historical calibration parameters, we cannot guarantee that subsequent ground images will automatically complete the matching and calibration process.

The above experiments indicate that the accuracies of the exterior and interior orientation parameters obtained by the star-based calibration are comparable to those of the ground-based calibration. And, compared to conventional ground-based method, the processing time and automation level of star-based method are greatly improved.

The method based on star observation has many advantages, and the Jilin-1 series high-resolution optical remote sensing satellites can achieve geometric calibration through this method. However, many satellites currently do not have such star observation conditions, mainly due to the following aspects. Firstly, this method requires satellites to have deep space imaging capabilities. In fact, if a satellite can observe moon, then this satellite can adjust its attitude to observe stars. Secondly, for optical satellites with imaging modes such as linear array push broom satellites, their star imaging methods

> REPLACE THIS LINE WITH YOUR MANUSCRIPT ID NUMBER (DOUBLE-CLICK HERE TO EDIT) <

are significantly different from those on the ground. It is necessary to adjust the exposure time of each line of the image and recalculate the rotation speed of the attitude during imaging. It is possible that even if the exposure time is increased to the maximum, it cannot photograph the star or can only photograph the brightest star, making it difficult to achieve interior

calibration. Finally, this article processed the attitude, but there were still some high-frequency attitude errors remaining, which resulted in an accuracy of 0.6 pixels for the validation scene S02. This requires higher frequency attitude measurement instruments to complete more precise attitude measurements and achieve higher calibration accuracy.

TABLE VIII
ERROR DISTRIBUTION STATISTICS OF G02 USING THE CALIBRATION PARAMETERS OF S01 AND G01

Images	Method	No. GCPs/CPs	Across track (meters)			Along track (meters)			Plane MSE (meters)
			MIN	MAX	RMSE	MIN	MAX	RMSE	
G02	S01 parameters	0/4255	-0.000	3.172	1.275	29.401	34.907	31.753	31.778
		4255/0	-0.003	-3.753	1.076	0.000	-2.162	0.583	1.224
	G01 parameters	0/4255	-0.001	-5.937	2.500	0.013	-59.043	30.892	30.993
		4255/0	0.004	3.116	0.988	0.006	1.731	0.642	1.178

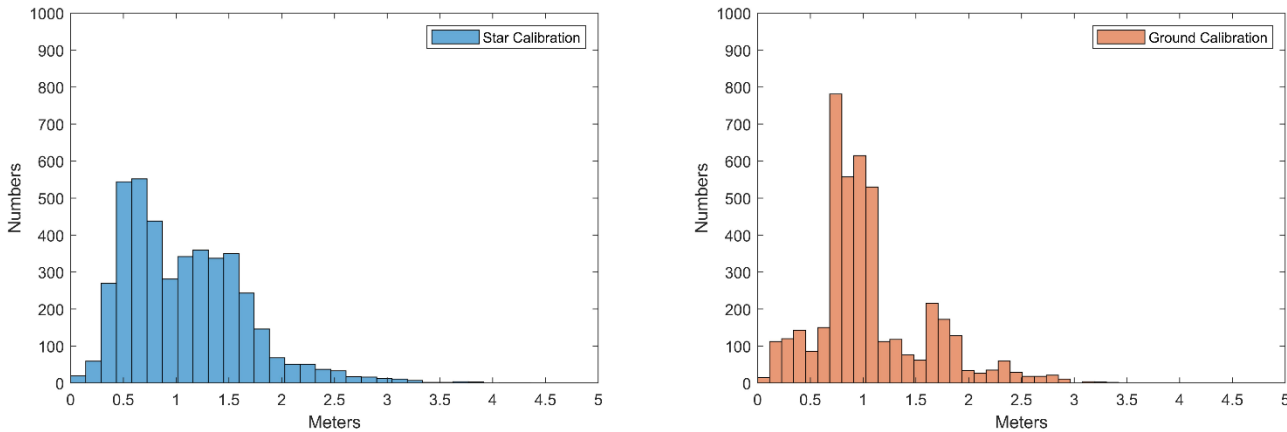


Fig. 14. Residual distribution map of G02 after star- and ground-based calibration

VI. CONCLUSION

In this study, the Jilin-1 satellite was used to photograph stars, and the geometric exterior and interior orientation parameters of the camera were calibrated using SCPs. With the multiple correction steps proposed in this study, the effects of image interior distortion and attitude errors were gradually eliminated, so that the geometric calibration accuracy of the image was better than 0.3 pixel. When another star image was used for verification, the geometric accuracy was better than 0.6 pixels. After ground image verification, the geometric positioning accuracy of the GF03D-03 satellite was 30 m without control. The interior orientation parameters obtained by the star-based calibration were applied to ground images with an interior accuracy of better than 1.5 m. The image corrected with the star-based calibration parameters was well overlaid on the reference image. The calibration parameters obtained by the star- and ground-based calibration field methods have similar accuracy verification results.

Most of the launched Jilin-1 satellites can observe stars, whereas other existing remote sensing satellites do not operate in this mode. Therefore, this method is currently not applicable to all satellites. Unlike ground-based calibration fields that have high maintenance cost and experience harsh imaging conditions, the star-based calibration mode does not need to consider the weather and climate on the ground and can capture images from

any location along the satellite orbit. As more and more constellations operate in the star observation mode in the future, the method proposed in this study will effectively reduce the geometric calibration time of satellites and effectively maintain the geometric accuracy of images throughout their in-orbit lifetime. In general, star-based calibration can meet the requirements for high-frequency geometric calibration of linear array cameras and provides an innovative method for geometric calibration of linear array satellite constellations. In future work, the use of star-based calibration to monitor the geometric accuracy of various satellites will be further discussed.

Declaration of interests statement

The authors declare that they have no known competing financial interests or personal relationships that could have appeared to influence the work reported in this paper.

Acknowledgements

The authors would like to thank the anonymous reviewers for their constructive comments and suggestions. This work has made use of data from the European Space Agency (ESA) mission Gaia (<https://www.cosmos.esa.int/gaia>), processed by the Gaia Data Processing and Analysis Consortium DPAC, (<https://www.cosmos.esa.int/web/gaia/dpac/consortium>). We would like to thank Editage (www.editage.cn) for English language editing.

> REPLACE THIS LINE WITH YOUR MANUSCRIPT ID NUMBER (DOUBLE-CLICK HERE TO EDIT) <

Funding

This work was supported by the National Natural Science Foundation of China [grant numbers 42301424, 42171341].

References

- [1] Zhang, Z., et al., 2023. Recent advances in using Chinese earth observation satellites for remote sensing of vegetation. *ISPRS J. Photogramm. Remote Sens.* 195, 393-407. <https://doi.org/10.1002/essoar.10510984.1>
- [2] Wang, J., et al., 2017. The on-orbit calibration of geometric parameters of the Tian-Hui 1 (TH-1) satellite. *ISPRS J. Photogramm. Remote Sens.* 124, 144-151. <https://doi.org/10.1016/j.isprsjprs.2017.01.003>
- [3] Wang, M., et al., 2017. On-orbit geometric calibration and geometric quality assessment for the high-resolution geostationary optical satellite GaoFen4. *ISPRS J. Photogramm. Remote Sens.* 125, 63-77. <https://doi.org/10.1016/j.isprsjprs.2017.01.004>
- [4] Zhang, G. and Guan, Z., 2018. Primary research on reliability of satellite imaging quality. *Geomatics and information science of Wuhan University* 43, 1954.
- [5] Guan, Z., et al., 2019. Star-based calibration of the installation between the camera and star sensor of the LuoJia 1-01 Satellite. *Remote Sensing (Basel, Switzerland)* 11(18), 2081. <https://doi.org/10.3390/rs11182081>
- [6] Jiao, N., et al., 2020. A generic framework for improving the geopositioning accuracy of multi-source optical and SAR imagery. *ISPRS J. Photogramm. Remote Sens.* 169, 377-388. <https://doi.org/10.1016/j.isprsjprs.2020.09.017>
- [7] Zhao T., et al., 2024. Artificial intelligence for geoscience: Progress, challenges and perspectives. *The Innovation* 5(5), 100691. <https://doi.org/10.1016/j.xinn.2024.100691>
- [8] Jiang, Y., et al., 2014. Geometric calibration and accuracy assessment of ZiYuan-3 multispectral images. *IEEE Trans. Geosci. Remote Sens.* 52(7), 4161-4172. <https://doi.org/10.1109/TGRS.2013.2280134>
- [9] Cao, J., X. Yuan and J. Gong, 2015. In-orbit geometric calibration and validation of ZY-3 three-line cameras based on CCD-detector look angles. *Photogramm. Rec.* 30(150), 211-226. <https://doi.org/10.1111/phor.12100>
- [10] Tang, X., et al., 2015. Verification of ZY-3 satellite imagery geometric accuracy without ground control points. *IEEE Geosci. Remote Sens. Lett.* 12(10), 2100-2104. <https://doi.org/10.1109/LGRS.2015.2450251>
- [11] Yang, B., et al., 2017. Large-scale block adjustment without use of ground control points based on the compensation of geometric calibration for ZY-3 images. *ISPRS J. Photogramm. Remote Sens.* 134, 1-14. <https://doi.org/10.1016/j.isprsjprs.2017.10.013>
- [12] Pi, Y., et al., 2017. On-orbit geometric calibration using a cross image pair for the linear sensor aboard the agile optical satellite. *IEEE Geosci. Remote Sens. Lett.* 14(7), 1176-1180. <https://doi.org/10.1109/LGRS.2017.2702139>
- [13] Zhang, G., Xu, K., and Huang, W., 2017. Auto-calibration of GF-1 WFV images using flat terrain. *ISPRS J. Photogramm. Remote Sens.* 134, 59-69. <https://doi.org/10.1016/j.isprsjprs.2017.10.009>
- [14] Jiang, Y., et al., 2018. CCD distortion calibration without accurate ground control data for pushbroom satellites. *ISPRS J. Photogramm. Remote Sens.* 142, 21-26. <https://doi.org/10.1016/j.isprsjprs.2018.05.008>
- [15] Jiang, Y.H., et al., 2018. In-orbit geometric calibration without accurate ground control data. *Photogramm. Eng. Remote Sensing* 84(8), 485-493. <https://doi.org/10.14358/PERS.84.8.485>
- [16] Yang, B., et al., 2020. Integrated geometric self-calibration of stereo cameras onboard the ZiYuan-3 satellite. *ISPRS J. Photogramm. Remote Sens.* 162, 173-183. <https://doi.org/10.1016/j.isprsjprs.2020.02.015>
- [17] Greslou, D., et al., 2012. Pleiades-HR innovative techniques for geometric image quality commissioning. 2012 XXII ISPRS Congress 543-547. <https://doi.org/10.5194/isprarchives-XXXIX-B1-543-2012>
- [18] Kubik, P., L.L.S.F., 2012. First in-flight results of Pleiades 1A innovative methods for optical calibration, in *International Conference on Space Optics*. Ajaccio Corse.
- [19] Amberg, V., et al., 2013. In-flight attitude perturbances estimation – Application to PLEIADES-HR satellites. *Proc Spie.* 8866(2), 206-209. <https://doi.org/10.1117/12.2023275>
- [20] Mignard, F., et al., 2018. Gaia Data Release 2. The celestial reference frame (Gaia-CRF2). *Astron. Astro.* 616. <https://doi.org/10.1051/0004-6361/201833955>
- [21] Meygret, A., et al., 2019. On-orbit star-based calibration and modulation transfer function measurements for PLEIADES high-resolution optical sensors. *IEEE Trans. Geosci. Remote Sens.* 57(8), 5525-5534. <https://doi.org/10.1109/TGRS.2019.2900026>
- [22] Guan, Z., Zhang, G., and Ge, L., 2020. Correction of camera interior orientation elements based on multi-frame star map. in *IGARSS 2020 - 2020 IEEE International Geoscience and Remote Sensing Symposium*. <https://doi.org/10.1109/IGARSS39084.2020.9323389>
- [23] Guan, Z., et al., 2022. Detection of the angle change between camera and star tracker based on star observation. *ISPRS Ann.* V-1-2022, 77--83. <https://doi.org/10.5194/isprs-annals-V-1-2022-77-2022>
- [24] Guan, Z., et al., Low-Frequency Attitude Error Compensation for the Jilin-1 Satellite Based on Star Observation, *IEEE Trans. Geosci. Remote*, 2023, 61, 1-17. <https://doi.org/10.1109/TGRS.2023.3274952>
- [25] Li, X., et al., 2019. A correction method for thermal deformation positioning error of geostationary optical payloads. *IEEE Trans. Geosci. Remote* 57(10), 7986-7994. <https://doi.org/10.1109/TGRS.2019.2917716>
- [26] Jiang, L., et al., 2021. On-orbit geometric calibration from the relative motion of stars for geostationary cameras. *Sensors* 21(19). <https://doi.org/10.3390/s21196668>
- [27] Chen, X., et al., 2021. On-orbit high-accuracy geometric calibration for remote sensing camera based on star sources observation. *IEEE Trans. Geosci. Remote* 1-11. <https://doi.org/10.1109/TGRS.2021.3100841>

> REPLACE THIS LINE WITH YOUR MANUSCRIPT ID NUMBER (DOUBLE-CLICK HERE TO EDIT) <



Zhichao Guan received the Ph.D. degree in Photogrammetry and Remote Sensing from LIESMARS, Wuhan University, Wuhan, China, in 2018. His doctoral dissertation focused on the elimination of attitude errors for high-resolution optical satellites.

He worked at LIESMARS, Wuhan University as a postdoc from 2018 to 2024. He has been working with NSMC, China Meteorological Administration since June 2024. His research interests include geometric positioning of remote sensing satellites and high-precision satellite attitude processing .



Guo Zhang received the B.E. and Ph.D. degrees in Photogrammetry and Remote Sensing from the School of Remote Sensing and Information Engineering, Wuhan University, Wuhan, China, in 2000 and 2005, respectively.

He has been working with LIESMARS, Wuhan University, since 2005, where he became a professor in 2011. His research interests include space photogrammetry, involving the processing and applications for optical load, synthetic aperture radar (SAR) load, video load, and laser load.



Yonghua Jiang received the Ph.D. degree in Photogrammetry and Remote Sensing from the LIESMARS, Wuhan University, Wuhan, China, in 2015. His doctoral dissertation focused on the elimination of high-frequency errors for high-resolution optical satellites.

He has been working with the School of Remote Sensing and Information Engineering, Wuhan University, since 2015. His research interests include geometry processing of space-borne optical imagery and high-accuracy image matching.



Xing Zhong received the Ph.D. degree in optical engineering from the Changchun Institute of Optics, Fine Mechanics and Physics (CIOMP), Changchun, China, in 2009.

He worked at CIOMP as an Associate Professor from 2009 to 2014. In 2015, he became a Full Professor at CIOMP and took part in the work for founding Chang Guang Satellite Technology Company Ltd. (CGSTL), Changchun. He is currently the Vice President and the Chief Engineer with CGSTL and a Professor at the University of Chinese Academy of Sciences, Beijing, China. His research interest is satellite's overall design, especially the payload and platform integration technologies.